

Biom mineralization

Zinc Phosphate Nanoparticles Produced in Saliva

Patrick E. J. Saloga,^[a,b] Glen J. Smales,^[a] Adam H. Clark,^[c] and Andreas F. Thünemann*^[a]

Abstract: This paper reports the formation of zinc phosphate nanoparticles from the artificial digestion of zinc chloride. Initially, the formation of amorphous primary particles with a mean radius of 1.1 nm is observed, alongside the formation of larger, protein stabilized aggregates. These aggregates, with a radius of gyration of 37 nm, are observed after 5 minutes of exposure to artificial saliva and are shown to be colloidally stable for a minimum time of two weeks. The initially formed primary particles are thought to consist of amorphous zinc phos-

phate, which is then transformed into crystalline $Zn_3(PO_4)_2 \cdot 4H_2O$ over the course of two weeks. Our results demonstrate that the interaction of inorganic salts with bodily fluids can induce the formation of de novo nanoparticles, which in turn, provides insights into how zinc-enriched foods may also facilitate the formation of nanoparticles upon contact with saliva. As such, this may be considered as an undesirable (bio)mineralization.

Introduction

Zinc salts are commonly added to food and cosmetic products to promote health and well-being, as zinc is an essential trace element required by the hundreds of different enzymes within the human body.^[1] The recommended daily zinc intake is 8–11 mg,^[2] and levels of zinc within the body are maintained predominantly through absorption and excretion within the gastrointestinal tract.^[3] Zinc salts, instead of elemental zinc, are added to products intended for human use/consumption, such as cereals and mouthwash, often in the form of compounds such as zinc acetate, zinc chloride, zinc gluconate and zinc glutamate.^[4] However, the use of zinc-enriched products can lead to the intake of excessive amounts of zinc (> 40 mg/day), which can induce adverse effects, such as dysfunctions of the gastrointestinal tract, or a reduced copper status.^[2] The achievement of daily intake levels > 300 mg with zinc-enriched, over-the-counter products has been reported to be potential causes of anaemia and leukopenia.^[5]

For these reasons, cosmetic products within the European Union, are only permitted to contain water-soluble zinc salts up to concentrations of 1 % to protect human health within the

Single Market.^[4] Recently, Voss et al.^[31] evaluated the environmental impact of ZnO nanoparticles by in vitro simulated digestion.

In this study, zinc chloride ($ZnCl_2$) at a mass fraction of ≈ 0.13 % in saliva, is utilized to study the effects that can occur upon its addition to saliva, and more precisely, evaluate whether the formation of nano-scale structures occurs. This is particularly relevant from a toxicological point of view where the chemical transformation, or the de novo formation of nanostructures with different toxicological properties to those of the originally ingested material, can take place.^[6]

Results

Formation of Nanoparticles

An aqueous solution of zinc chloride (sample A) was added to a solution of artificial saliva (sample B), which abides by the German standard DIN 19378.^[7] As per the NANOGENOTOX protocol for producing suitable, manufactured nanomaterial exposure media, the artificial saliva contained the protein bovine serum albumin (BSA).^[8]

The samples were examined after the addition of the zinc salt to artificial saliva at time intervals of five minutes (sample C), seven hours (sample D), and after a period of storage of two weeks (sample E).


For the investigation of the samples in a size range of approximately 0.3 - 300 nm, small-angle X-ray scattering (SAXS) was utilized as a method of choice, in combination with wide-angle X-ray scattering (WAXS) to detect changes in crystalline structures. Sample B was used as background, for which the SAXS data of samples C, D, and E was corrected (see Figure S1, Supporting Information).


We found that the intensity of the SAXS signal increases rapidly upon the addition of $ZnCl_2$ to artificial saliva, and upon investigation of sample C, the scattering curve exhibits features

[a] P. E. J. Saloga, Dr. G. J. Smales, Dr. A. F. Thünemann
Bundesanstalt für Materialforschung und -prüfung (BAM),
Unter den Eichen 87, 12205 Berlin, Germany
E-mail: andreas.thuenemann@bam.de

[b] P. E. J. Saloga
Freie Universität Berlin, Fachbereich Biologie, Chemie, Pharmazie,
Takustraße 3, 14195 Berlin, Germany

[c] Dr. A. H. Clark
Paul Scherrer Institut,
Forschungsstrasse 111, 5232 Villigen PSI, Switzerland

 Supporting information and ORCID(s) from the author(s) for this article are available on the WWW under <https://doi.org/10.1002/ejic.202000521>.

 © 2020 The Authors. Published by Wiley-VCH Verlag GmbH & Co. KGaA. This is an open access article under the terms of the Creative Commons Attribution License, which permits use, distribution and reproduction in any medium, provided the original work is properly cited.

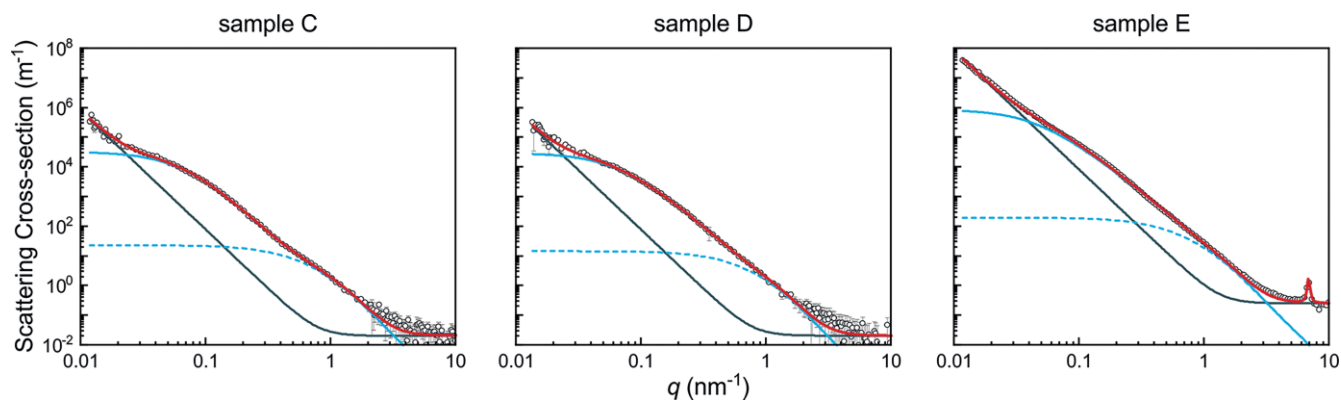


Figure 1. SAXS data of samples C, D, and E (symbols). The model curves (red, solid lines) are the sum of the scattering contribution from the particles according to Equation (1) (blue, solid lines) and a background according to Equation (2) (gray lines). The particle scattering is the product of the form factor of log-normally distributed spheres according to Equation (3) (blue dashed lines) and the mass fractal structure factor according to Equation (7). The structure factors are depicted in Figure S2 (Supporting Information).

typically expected from the presence of nano-scale structures (see Figure 1).

The SAXS pattern can be described well by the presence of two populations of nanostructures from the bumps observed in the data at q -values of ca. 0.1 and 1 nm^{-1} . Due to this, the scattering curves are modelled as the sum of a contribution from small primary particles that form aggregates (mass fractal agglomerates),^[9,10] alongside a contribution from larger particles with radii of several hundred nanometers, due to the SAXS patterns' tendency towards a slope of q^{-4} at low q -values.

Briefly, the scattering intensity $I(q)$ as a function of the scattering vector q is the product of the particle form factor $P(q)$ and the structure factor $S(q)$, and it is complemented by a background function according to Equations (1) and (2).

$$I(q) = P(q)S(q) + I_{\text{bkg}}(q) \quad (1)$$

$$I_{\text{bkg}}(q) = a + bq^{-4} \quad (2)$$

$I_{\text{bkg}}(q)$ was introduced to compensate for structures larger than ca. 300 nm in radius, whose scattering signal – as a first approximation – was expected to drop off with q^{-4} in the q -range under investigation.

The form factor of a log-normal size distribution of spherical particles is composed of said size distribution $f(N, R, R_{\text{median}}, \sigma_{\log})$ and the scattering from a single sphere $I_s(\Delta\eta, q, R)$ in Equation (3) as:

$$P(q) = \int_0^\infty f(N, R, R_{\text{median}}, \sigma_{\log}) I_s(\Delta\eta, q, R) dR. \quad (3)$$

Here, N is the particle number density, R the sphere radius, R_{median} the median sphere radius, σ_{\log} the width parameter of the size distribution, and $\Delta\eta$ the scattering length density difference between the particles and the surrounding medium. The log-normal size distribution is defined as Equation (4):

$$f(N, R, R_{\text{median}}, \sigma_{\log}) = \frac{N}{R\sigma_{\log}\sqrt{2\pi}} \exp\left[-\frac{(\ln R - \ln R_{\text{median}})^2}{2\sigma_{\log}^2}\right] \quad (4)$$

and the scattering of a single sphere as Equation (5):

$$I_s(\Delta\eta, q, R) = \left[\frac{4}{3}\pi R^3 \Delta\eta \frac{3(\sin qR - qR \cos qR)}{(qR)^3}\right]^2. \quad (5)$$

$P(q)$ is depicted in Figure 1 as the blue, dashed line and corresponds to the scattering of non-interacting particles, i.e. $S(q) = 1$. The corresponding number density of particles N and the size distribution parameters R_{median} , and σ_{\log} can be found in Table S1 (Supporting Information). From these values, the mean radius R_{mean} and the width σ of the size distribution were calculated in Equation (6):

$$R_{\text{mean}} = R_{\text{median}} e^{\frac{\sigma_{\log}^2}{2}} \text{ and } \sigma = R_{\text{mean}} \left(e^{2\sigma_{\log}^2} - e^{\sigma_{\log}^2}\right)^{\frac{1}{2}}. \quad (6)$$

To include particle–particle interactions such as the formation of agglomerates, a q -dependent structure factor needs to be introduced. Equation (7) depicts the structure factor of said mass fractal, with the fractal dimension D , the mean radius of the individual particles r_0 , the distance from the fractal center r , and the fractal correlation cut-off ξ . In general, r_0 can be interpreted as the particle radius including any stabilizing shell separating the individual particles, and ξ as the fractal aggregate radius.^[9,10] The structure factors as a function of the scattering vector are depicted in Figure S2 (Supporting Information).

$$S(q) = 1 + \frac{D}{r_0} \int_0^\infty r^{D-1} \exp\left[-\frac{r}{\xi}\right] \frac{\sin qr}{qr} dr. \quad (7)$$

The integral in $S(q)$ can be solved analytically according to Equation (8):

$$S(q) = 1 + \frac{D\Gamma(D-1) \sin[(D-1) \arctan q\xi]}{(qr_0)^D [1+(q\xi)^2]^{(D-1)/2}}. \quad (8)$$

Multiplication of the structure factor with the form factor as in Equation (1) yields the scattering intensity $I(q)$ of an aggregate consisting of log-normally distributed spherical particles, and is depicted in Figure 1 as the blue, solid line. That way, the parameters of the mass fractal r_0 , ξ , and D were obtained.

Furthermore, the radius of gyration R_g and the aggregation number N_{agg} were determined in Equation (9) as:

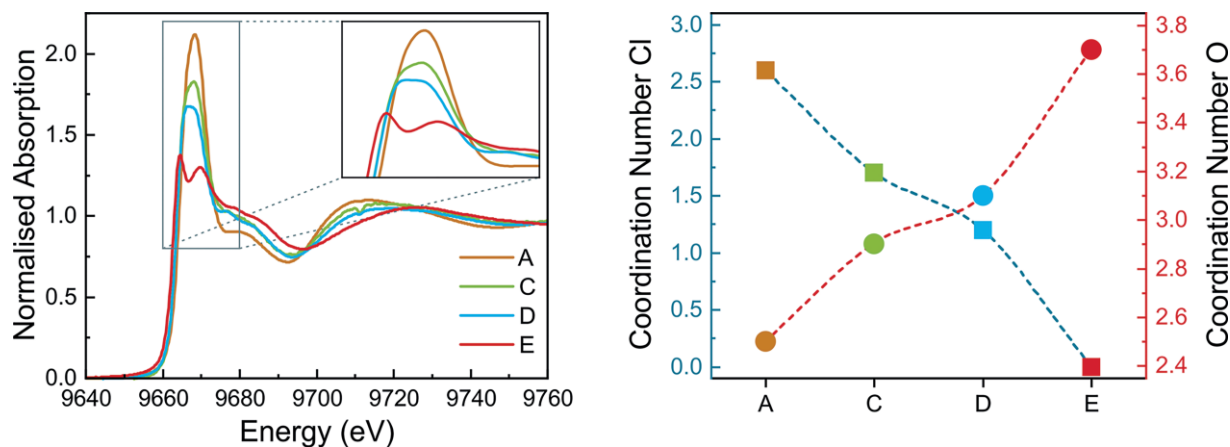


Figure 2. X-ray absorption fine structure (XAFS) spectra measured at the Zn *K*-edge of samples A, C, D, and E (left, solid lines), and coordination numbers of zinc (right) with regard to chlorine (squares, left axis of ordinate) and oxygen (circles, right axis of ordinate) as determined from fitting to the EXAFS region.

$$R_g = \xi \left[\frac{1}{2} D(D+1) \right]^{\frac{1}{2}} \text{ and } N_{\text{agg}} = \left(\frac{R_g}{r_0} \right)^D \quad (9)$$

The particle size distribution parameters obtained from the aforementioned theory can be found in Table S1 (Supporting Information).

X-ray Absorption Spectroscopy

X-ray absorption spectroscopy (XAS) measurements were carried out to investigate the local structural environment of zinc within the reaction medium. The X-ray absorption fine structure (XAFS) of the zinc-containing samples (A, C, D, and E) at the Zn *K*-edge (9660 eV) is shown in Figure 2 (left), with the refined Zn–Cl and Zn–O coordination numbers (right) obtained from fitting of the extended X-ray absorption fine structure (EXAFS). The X-ray absorption near edge structure (XANES) is shown with an enlarged inset focusing on the top of the edge (left). EXAFS fitting was performed with k^2 weighting between 2.1 and 10.3 Å⁻¹ to refine the local geometric structure. The quality of the EXAFS fitting is shown in Figure S3 (Supporting Information) for both *R*- and *k*-spaces, demonstrating a close agreement between the model and the data for all samples. The bond length of Zn–O and Zn–Cl refined to be approximately 1.94 Å and 2.36 Å which are in line with the structure of ZnO and ZnCl₂ respectively.

Compound Identification

Infrared spectroscopy (IR) and wide-angle X-ray scattering (WAXS) were employed to determine the chemical composition of the nanostructures formed in the digestive process. Since after combining aqueous solutions of ZnCl₂ and the respective component of saliva (see Table 1), formation of a precipitate was only evident in the cases of KH₂PO₄ and NaHCO₃, these samples were selected for comparison with sample C (ZnCl₂ in saliva). IR spectra were recorded and are depicted in Figure 3, and WAXS data is displayed in Figure 4, alongside reference

data for CaSO₄·2H₂O and Zn₃(PO₄)₂·4H₂O, taken from ICSD Collection Codes 161622^[11] and 1945.^[12]

Table 1. Composition of artificial saliva.

Compound	Supplier	Amount [mg]
α-Amylase	Sigma-Aldrich	41.9
CaCl ₂ ·2H ₂ O	NeoLab	25.0
KCl	NeoLab	75.0
KH ₂ PO ₄	AppliChem	100.0
Mucin	Sigma-Aldrich	125.3
NaCl	NeoLab	83.4
NaHCO ₃	NeoLab	25.0
NaSCN	Carl Roth	25.0
Na ₂ SO ₄ ·10H ₂ O	AppliChem	207.9
Urea	AppliChem	1.7
Uric acid	AppliChem	16.7

Discussion

To elucidate whether the addition of an aqueous solution of ZnCl₂ to artificial saliva could induce the formation of nanostructures, a corresponding solution was characterized by means of SAXS, XAFS, WAXS, and IR at three time points throughout the digestion procedure. In total, the following five samples were obtained and examined: 6.8 % ZnCl₂ in H₂O before the addition to saliva (sample A), artificial saliva without zinc (sample B), and 0.13 % ZnCl₂ in saliva after five minutes (sample C), seven hours (sample D), and after a storage period of two weeks (sample E). SAXS curves were obtained from samples B, C, D, and E, with sample B acting as a background correction for the other three samples. XAFS measurements were performed on the zinc-containing samples A, C, D, and E, whilst WAXS measurements were performed on all samples. The identification of the products formed was complemented by IR measurements of sample C.

It may also be desirable to additionally characterize the samples with imaging techniques, such as SEM and TEM, however, saliva does not conform well to such methods due to its high content of salts and proteins.

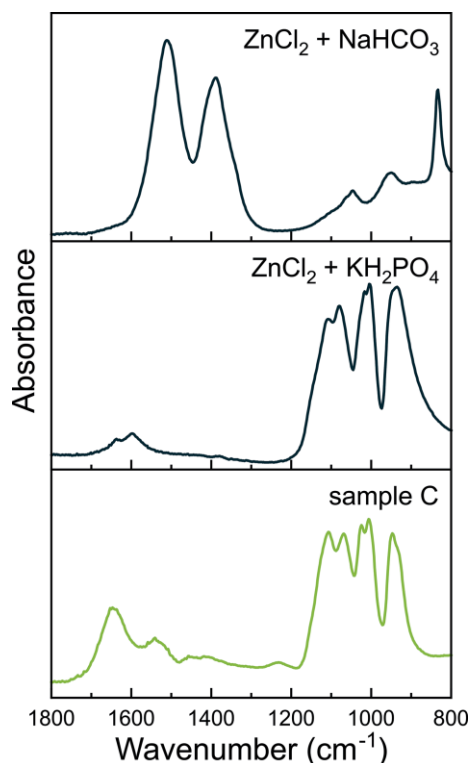


Figure 3. Infrared absorbance spectra of the precipitate formed from ZnCl_2 in aqueous solutions of NaHCO_3 (top), KH_2PO_4 (middle), and in saliva (bottom). The top spectrum shows absorption bands characteristic of the carbonate ion (antisymmetric stretching modes at $\tilde{\nu} = 1513 \text{ cm}^{-1}$ and 1388 cm^{-1} , symmetric stretching mode at $\tilde{\nu} = 1054 \text{ cm}^{-1}$, and bending modes at $\tilde{\nu} = 953 \text{ cm}^{-1}$ and 832 cm^{-1}). The two remaining spectra show absorption bands associated with the phosphate ion (symmetric and antisymmetric stretching modes between $\tilde{\nu} = 800 \text{ cm}^{-1}$ and 1200 cm^{-1}) and water of hydration (bending modes around $\tilde{\nu} = 1600 \text{ cm}^{-1}$).

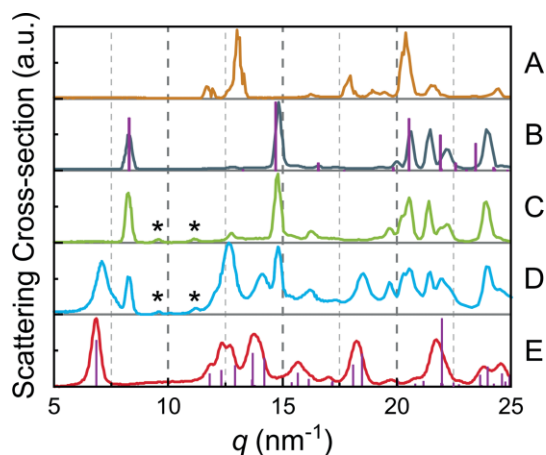


Figure 4. Wide-angle X-ray scattering data of samples A–E (solid lines) and reference data for $\text{CaSO}_4 \cdot 2\text{H}_2\text{O}$ (bars at sample B) and $\text{Zn}_3(\text{PO}_4)_2 \cdot 4\text{H}_2\text{O}$ (bars at sample E), taken from ICSD Collection Codes 161622^[11] and 1945^[12] respectively.

From SAXS measurements, the formation of nanoparticles was observed within five minutes of incubation in artificial saliva. Small primary particles, exhibiting a mean radius of $R_{\text{mean}} = 1.1 \pm 0.2 \text{ nm}$ and a distribution width of $\sigma = 0.7 \pm 0.2 \text{ nm}$, were

found to aggregate, alongside structures larger than the maximum visible range of the data (ca. 300 nm in radius) in samples C, D, and E. From fits of the SAXS data, it can be seen that the resulting parameters describing the primary particles remained unchanged, within their relative uncertainties, throughout the experiments (samples C, D and E). This gives a good indication that the primary particles are present from the beginning, with their size distribution not changing significantly over the remaining period. Hence, only changes in the chemical composition and interaction with the environment are thought to be possible.

Within the scope of identifying the chemical composition of the formed particles, infrared spectroscopy measurements revealed similarities between the precipitates formed from ZnCl_2 with KH_2PO_4 and in saliva whilst the sample formed in the presence of NaHCO_3 is substantially different (Figure 3). More specifically, the latter displayed strong absorption bands at $\tilde{\nu} = 1513 \text{ cm}^{-1}$ and 1388 cm^{-1} , which are associated with the antisymmetric stretching modes of the carbonate ion.^[13] Bands stemming from the symmetric stretching mode (1054 cm^{-1}) and the bending modes (953 cm^{-1} and 832 cm^{-1}) are also observed. Hales and Frost performed infrared spectroscopy studies on smithsonite (ZnCO_3) and hydrozincite [$\text{Zn}_5(\text{CO}_3)_2(\text{OH})_6$]. They attributed the occurrence of the otherwise IR-inactive symmetric stretching mode and of several antisymmetric stretching modes in hydrozincite to the reduced symmetry as compared to smithsonite.

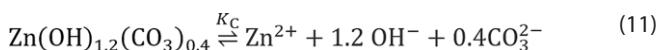
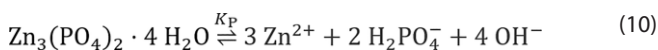
The other two samples, on the other hand, show several bands in the $800 \text{ cm}^{-1} - 1200 \text{ cm}^{-1}$ -region that are typical for the phosphate ion and assigned to symmetric and antisymmetric stretching modes.^[14] The broader, less pronounced bands around 1600 cm^{-1} are thought to originate from bending modes of water of hydration. Therefore, it was assumed that a hydrated zinc phosphate forms upon the addition of ZnCl_2 to saliva and wide-angle X-ray scattering (WAXS) measurements of the dried samples A–E were carried out (Figure 4).

As a reference, the scattering pattern of ZnCl_2 was collected (sample A), however this characteristic signal is not found in the subsequent samples, indicating that the compound has undergone a chemical transformation. Upon centrifugation and drying of the artificial saliva (sample B), scattering peaks of $\text{CaSO}_4 \cdot 2\text{H}_2\text{O}$ became visible at $q = 8.28 \text{ nm}^{-1}$, 14.84 nm^{-1} , 16.55 nm^{-1} , and in the region of $q > 20 \text{ nm}^{-1}$. These peaks remained visible in subsequent samples C and D. $\text{CaSO}_4 \cdot 2\text{H}_2\text{O}$ is thought to have formed due to the presence of $\text{CaCl}_2 \cdot 2\text{H}_2\text{O}$ and $\text{Na}_2\text{SO}_4 \cdot 10\text{H}_2\text{O}$ in saliva, and has been identified by comparison to a reference pattern (bars at sample B, ICSD collection code 161622).^[11] The signal from $\text{CaSO}_4 \cdot 2\text{H}_2\text{O}$ is seen to dominate the pattern obtained from sample C, suggesting that shortly after the injection of the ZnCl_2 solution, no considerable amounts of other crystalline material were formed. However, small, broad diffraction peaks at $q = 9.56 \text{ nm}^{-1}$ and 11.16 nm^{-1} were observed in both sample C and D (asterisks), but not in the final product (sample E). This may indicate the formation of an intermediate, thought to be hydrozincite [$\text{Zn}_5(\text{CO}_3)_2(\text{OH})_6$], which exhibits diffraction peaks at similar positions (ICSD collection code 16583).^[15] Shifts in the X-ray absorption near edge

fine structure (XANES) region of the X-ray absorption spectra (XAS) data support this assumption, as discussed later in more detail. Seven hours after the ZnCl_2 injection, besides scattering peaks of $\text{CaCl}_2 \cdot 2\text{H}_2\text{O}$, those of the final product $\text{Zn}_3(\text{PO}_4)_2 \cdot 4\text{H}_2\text{O}$ became visible in the WAXS pattern of the dried sample D, although slightly shifted to higher q -values. For instance, the (020) scattering peak appeared at $q = 7.11 \text{ nm}^{-1}$ and was observed to be broadened in comparison to that seen in sample E at $q = 6.83 \text{ nm}^{-1}$. In comparison to the SAXS curves of the liquid samples D and E, it can be seen that the said scattering peak is only visible in sample E, with the diffraction signal most likely being masked by the scattering of water in sample D.

Scattering of $\text{Zn}_3(\text{PO}_4)_2 \cdot 4\text{H}_2\text{O}$ was not observed in sample C, and non-crystalline intermediates during the formation of zinc phosphate have been reported in the literature. For instance, Roming et al. reported on the presence of non-crystalline zinc phosphate structures in nanoparticles obtained from a polyol-mediated synthesis.^[16] Despite the application of a whole series of analytical methods, such as solid state P-NMR, they were unable to elucidate the structure exactly. However, the presence of a low-molecular organic compound (diethylene glycol) in the structure are thought to be responsible for the observed delay in crystallization. Similarly, in an elaborate study by Bach et al., the presence of non-crystalline zinc phosphate nanoparticles as intermediate species, during the formation of crystalline zinc phosphate hydrates, was confirmed.^[17] This is consistent with the observed delay, of more than 24 hours, for the appearance of Bragg reflections in a BSA-templated synthesis of zinc phosphate nanocomposites, as reported by Song et al.^[18] Therefore, we speculate that the particles observed in sample C initially consist of a non-crystalline zinc phosphate and, similar to that reported by Roming et al., exhibit a significant delay in crystallization due to organic components of the artificial saliva. Lastly, the WAXS pattern of sample E was only indicative of the formation of $\text{Zn}_3(\text{PO}_4)_2 \cdot 4\text{H}_2\text{O}$ and no signals of ZnCl_2 , $\text{CaCl}_2 \cdot 2\text{H}_2\text{O}$, or the possible intermediates were found, indicating that the chemical transformation from ZnCl_2 to $\text{Zn}_3(\text{PO}_4)_2 \cdot 4\text{H}_2\text{O}$ was only complete after the storage period of two weeks. Based on the described results of the WAXS and XAFS investigations, it is assumed that this transformation proceeds via precursors of amorphous zinc phosphate and hydrozincite, both compounds being sparingly soluble in water.

The formation of $\text{Zn}_3(\text{PO}_4)_2 \cdot 4\text{H}_2\text{O}$ instead of $\text{Zn}_5(\text{CO}_3)_2(\text{OH})_6$ as the final product is in accordance with the respective solubility values reported in literature: For the dissolution of $\text{Zn}_3(\text{PO}_4)_2 \cdot 4\text{H}_2\text{O}$ according to Equation (10), Nriagu^[19] found a solubility product constant K_P in the order of $10^{-52.2} \text{ M}^9$ while for the dissolution of $\text{Zn}_5(\text{CO}_3)_2(\text{OH})_6$ according to Equation (11), a K_C of $10^{-14.9} \text{ M}^{2.6}$ can be found.^[20] K_P and K_C can be converted to molar solubilities S_P and S_C according to Equation (12) and Equation (13), respectively.



From the resultant values of $S_P = 5 \times 10^{-7} \text{ M}$ and $S_C = 2.5 \times 10^{-6} \text{ M}$, the lower solubility of $\text{Zn}_3(\text{PO}_4)_2 \cdot 4\text{H}_2\text{O}$ compared

$$K_P = (3S_P)^3(2S_P)^2(4S_P)^4 \Leftrightarrow S_P = (K_P/27648)^{1/9} \quad (12)$$

$$K_C = S_C(1.2S_C)^{1.2}(0.4S_C)^{0.4} \Leftrightarrow S_C = (K_C/0.48)^{1/2.6} \quad (13)$$

to $\text{Zn}_5(\text{CO}_3)_2(\text{OH})_6$ becomes apparent, which implies a preferred formation of the phosphate.

A deeper insight into the changes in chemical composition and crystal structure was obtained by XAFS. Zinc is most commonly found in the +II oxidation state, with only rare cases of Zn^{I} , found within compounds featuring Zn–Zn-bonds.^[21] XAFS experiments confirmed the presence of Zn^{II} within the sample and provided evidence that during the artificial digestion of ZnCl_2 no Zn^{I} species are formed.

A decrease in intensity of the absorption edge over time is clearly visible (enlarged in the inset of Figure 2). The single peak observed from sample A at an energy of $9668 \pm 1 \text{ eV}$, slowly decreases and splits into two distinct absorption peaks within the edge region at $9664 \pm 1 \text{ eV}$ and $9670 \pm 1 \text{ eV}$. Furthermore, a less pronounced feature directly after the white line develops at $9677 \pm 1 \text{ eV}$. Immediately after the injection of ZnCl_2 into artificial saliva (sample C), the Zn K -edge is significantly altered and shows decreasing white line intensity, a trend that progresses during the following seven hours, until sample D is obtained. After storage, the white line intensity is further reduced, whilst a doublet forms near the top of the edge in sample E, which is in accordance with the XANES investigations of mineral and synthetic zinc phosphate hydrates undertaken by Castorina et al.^[22] Regarding sample A as the precursor and sample E as the end product, the inset of Figure 2 shows that upon injection of ZnCl_2 , a quick transformation to sample C occurs, whilst the following change via sample D to the product, is much slower. It can also be noted that there are no isosbestic points in the XANES region, demonstrating the potential presence of an unidentified intermediate. Hence, linear combination fitting of the precursor and product to provide further insight into the XANES data is not possible here. Thus, the XANES data supports the assumption previously raised of the transient formation of another zinc compound such as $\text{Zn}_5(\text{CO}_3)_2(\text{OH})_6$.

EXAFS analysis was performed to follow the change in local coordination around Zn to gain additional insight. With regard to the coordination numbers of zinc in relation to chlorine and oxygen, it can be seen that the former is constantly increasing over time, whilst the latter is decreasing. It is known, from the literature, that ZnCl_2 can dissociate completely at low concentrations in aqueous solution.^[23] In the presence of water, Zn^{2+} can coordinate octahedrally, whilst also remaining coordinated to Cl^- at higher concentrations, explaining the higher coordination number of Zn^{2+} in relation to Cl^- observed in sample A. The results from EXAFS fitting are given in Table S2 (Supporting Information). Due to high correlation with coordination number, the Debye–Waller factors σ^2 were held constant after refinement from the ZnCl_2 precursor. The Zn–Cl bond length was constrained for sample E due to the lack of contribution to the EXAFS. All other parameters were freely refined.

Based on the XAS and WAXS investigations, we assume an initial formation of amorphous zinc phosphate, with the partici-

pation of hydrozincite as an intermediate, being a similarly sparingly soluble compound, but not the most thermodynamically stable. Subsequently, the conversion to crystalline $\text{Zn}_3(\text{PO}_4)_2 \cdot 4\text{H}_2\text{O}$ proceeds over a period of two weeks, however definitive statements about the kinetics of particle formation go beyond the scope of this study.

Examining further structural parameters obtained from SAXS analysis, the particle number densities N of the primary particles is seen to remain unchanged within uncertainties in samples C and D (at $5.2 \pm 0.1 \times 10^{15} \text{ mL}^{-1}$, and $4.6 \pm 0.6 \times 10^{15} \text{ mL}^{-1}$, respectively). After two weeks of storage (sample E), a near 20-fold increase in the primary particle number density to $80.6 \pm 0.2 \times 10^{15} \text{ mL}^{-1}$ is observed.

Particle–particle interactions are represented in SAXS curve fitting by the structure factor, yielding information on the aggregates formed, such as aggregation number N_{agg} , radius of gyration R_g , aggregate radius ξ , and the radius of the single objects within the aggregates r_0 . The latter is not to be confused with the mean particle radius R_{mean} , as in the case of particles surrounded by a shell of lower scattering contrast, R_{mean} may not include said shell in contrast to r_0 .

In all cases, the mean radius of the particle cores R_{mean} was smaller than the core/shell radius r_0 , indicating that within the aggregates formed, particles were separated and stabilized by an intermediate layer, which was assumed to be made up from protein found within the artificial saliva. More specifically, the samples contained α -amylase, BSA, as well as mucin (highly glycosylated proteins). BSA, for instance, is known to possess several cation binding sites, which can be formed by aromatic amino acid residues, and is used in the templated synthesis of inorganic nanostructures.^[18,24,25] However, more precise statements regarding the participation of the proteins present in the saliva samples in the nanostructure formation cannot be made at this point due to the high complexity of the reaction media. The structural parameters describing the primary particles aggregating changed over time: mean core/shell radii decreased significantly, from $r_0 = 2.2 \pm 0.2 \text{ nm}$ to $1.7 \pm 0.1 \text{ nm}$, during the first seven hours of incubation time between the collection of samples C and D, and remained the same within uncertainties during the following storage over two weeks yielding sample E. This indicates a likewise change of the thickness of the stabilizing shell, i.e. the particles became more tightly packed alongside their transformation into crystalline zinc phosphate.

Contrary, aggregate radius ξ , radius of gyration R_g , and aggregation number N_{agg} did only change significantly during the period of storage between collection of samples D and E. It was found that the aggregate radius increased from $\xi = 15.7 \pm 0.2 \text{ nm}$ in sample D to $22.4 \pm 0.1 \text{ nm}$ in sample E, which is reflected in likewise increasing radii of gyration (from $R_g = 36 \pm 1 \text{ nm}$ to $49 \pm 1 \text{ nm}$) and aggregation numbers (from $N_{\text{agg}} = 4400 \pm 200$ to 9000 ± 100). These observations indicate that during the first seven hours, in which the transformation of ZnCl_2 into crystalline $\text{Zn}_3(\text{PO}_4)_2 \cdot 4\text{H}_2\text{O}$ occurs, only the particle concentration within the aggregates increased. In contrast, the particles remained unchanged during subsequent storage, while the aggregates grew in size and approximately 20-fold in number density.

Conclusion

Upon the addition of ZnCl_2 to artificial saliva, nanoparticles with a mean radius of $1.1 \pm 0.2 \text{ nm}$ and a size distribution width of $0.7 \pm 0.2 \text{ nm}$ were observed, and they formed aggregates with radii of gyration of $37 \pm 1 \text{ nm}$, as determined from SAXS. Within these aggregates, the particles are thought to adhere via a shell of the protein found within artificial saliva. The initial composition of these nascent particles could not be determined directly, however, they were converted to $\text{Zn}_3(\text{PO}_4)_2 \cdot 4\text{H}_2\text{O}$ within seven hours of incubation, alongside an intermediate species [thought to be $\text{Zn}_5(\text{CO}_3)_2(\text{OH})_6$]. Comparisons to literature studies suggests that the primary particles consist of amorphous zinc phosphate precursors, and throughout the incubation period, these slowly form crystalline $\text{Zn}_3(\text{PO}_4)_2 \cdot 4\text{H}_2\text{O}$.

The changes in particle size distribution parameters of primary particles and their aggregates at incubation times of five minutes, seven hours and after a period of storage of two weeks are depicted in Figure 5. During the incubation period, the particle number density remained essentially the same (within uncertainties), whilst the aggregates became more tightly packed, i.e. the thickness of the particle-surrounding shell decreased. Meanwhile, the chemical transformation of ZnCl_2 into $\text{Zn}_3(\text{PO}_4)_2 \cdot 4\text{H}_2\text{O}$ proceeded with the involvement of an intermediate. In the subsequent storage period of two weeks, the particle number concentration increased about 20-fold as the aggregates grew. While they initially consisted of 3200 ± 900 primary particles, the aggregation number after storage was 9000 ± 100 . Thus, it was demonstrated that upon contact of solubilized, ionic zinc to artificial saliva, small $\text{Zn}_3(\text{PO}_4)_2 \cdot 4\text{H}_2\text{O}$ nanoparticles can be formed.

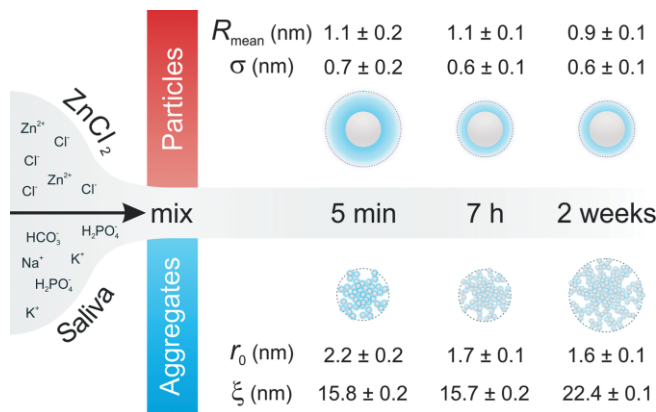


Figure 5. Scheme depicting the changes in particle size distribution parameters of primary particles and their aggregates over time, regarding mean particle core radius, R_{mean} , size distribution width, σ , mean particle core/shell radius, r_0 , and aggregate radius, ξ .

The assumption that the proteins, within the saliva, temporarily stabilize zinc phosphate nanoparticles seems rational as it is well-known that proteins have previously been utilized as colloidal stabilizers in the preparation of inorganic nanoparticles.^[18,24,25] Therein, proteins are frequently used in biotemplated nanoparticle synthesis. Most frequently used is BSA, which in our study is present in saliva at a concentration of 0.48 g L^{-1} . As an example, the production of a BSA templated

zinc phosphate $\text{Zn}_3(\text{PO}_4)_2$ @BSA was reported by Song et al.^[18] Their study reviews the biotemplated synthesis of metal phosphates, most of which were synthesized for application in catalysis.

In contrast, the particles of our study are not foreseen for technical applications. On the other hand, regularization of crystal formation is hotly debated in biomineralization. Therein, it is evident that proteins play a substantial role in healthy mineralization such as amorphous calcium phosphate in bone growth but also in pathological mineralization.^[26] Examples for undesired biominerals are kidney stones, atheromatous plaque and dental calculus. The zinc phosphate formation of our present study also has an amorphous initial state as it seems to be a typical phenomenon in biomineralization. For example, Gebauer et al. were the first to discover that stable prenucleation clusters play an important role as intermediate species in the crystallization of calcium carbonate.^[27]

In conclusion, the zinc phosphate nanoparticles may also form in vivo if food and cosmetics products, containing the permitted zinc salt concentrations, are ingested, which could be a source of unintentional mineral formation. Similarly, these results may be of relevance for the design of biological studies involving the use of, for example, ionic zinc and phosphate-containing buffers.

Experimental Section

Materials

Zinc(II) chloride (ZnCl_2) was purchased from Merck, bovine serum albumin (BSA) from Sigma-Aldrich and all chemicals for artificial saliva from AppliChem, Carl Roth, NeoLab or Sigma-Aldrich according to Table 1. Ultrapure water (*Milli-Q*, 18.2 $\text{M}\Omega\cdot\text{cm}$ at 25 °C) was used.

Artificial Saliva

We adapted an in vitro artificial digestion procedure based on the German standard DIN 19378.^[7] Solutions of ZnCl_2 (68.1 mg, sample A) and BSA (25 mg), in 1 mL of ultrapure water, respectively, were added to 50 mL of artificial saliva (composed according to Table 1, pH = 6.4 ± 0.05 , artificial saliva with BSA is referred to as sample B) and incubated at 37 °C for 5 min (sample C). Further samples were taken after 7 h incubation time (sample D) and after a period of storage at ca. 4 °C of two weeks (sample E).

SAXS/WAXS Measurements

Small- and wide-angle X-ray scattering (SAXS/WAXS) measurements were performed on a customized Xeuss 2.0 (Xenocs, France). X-rays were generated from a microfocus X-ray tube with a copper target, and a multilayer optic was employed to parallelize and monochromatize the beam to the $\text{Cu-K}\alpha$ wavelength of 0.1542 nm. The liquid samples were examined in flow by continuous pumping through a cell bearing silicon nitride windows. Data collection was performed using an in-vacuum Eiger 1M detector (Dectris, Switzerland) which was placed at multiple distances between 51–2507 mm from the sample. The resulting data has been processed and scaled to absolute units using the DAWN software package according to standardized procedures.^[28,29]

XAS Measurements

XAS measurements were carried out at the SuperXAS beamline of the Swiss Light Source. The storage ring operated at 2.4 GeV in top-up mode with a ring current of 400 mA. The polychromatic X-ray beam resulting from a 2.9 Tesla bending magnet was collimated by a silicon-coated mirror at 2.5 mrad (which also served to reduce higher-order harmonics) and subsequently monochromatized by a Si(111) channel-cut monochromator, which allowed data collection in quick-scanning extended X-ray absorption fine-structure spectroscopy (QEXAFS) at 1 Hz. The beam was focused using a Rh coated toroidal mirror with a focal spot size of $1000 \times 200 \mu\text{m}$. Spectra were collected in transmission mode using 15 cm long, 2 bar N_2 -filled ionization chambers. A Zn reference foil mounted between the second and third ionization chamber was measured simultaneously for absolute energy calibration. The QEXAFS spectra were processed using ProQEXAFS to extract individual XAS spectra,^[32] calibrate and normalize. Due to the inherent oversampling of the XAS spectra, radial basis function interpolation was employed to reduce the data point density. In the XANES region an energy step of 0.25 eV was used. In the EXAFS region a constant k -step of 0.025 \AA^{-1} was chosen. Fitting of the EXAFS was performed using the Demeter software package.^[30]

Acknowledgments

Open access funding enabled and organized by Projekt DEAL.

Keywords: Biomineralization · Nanoparticles · Structure elucidation · Zinc · Artificial digestion

- [1] C. J. Boreiko, *J. Toxicol. Environ. Health Part A* **2010**, *73*, 166–174.
- [2] *Institute of Medicine, Dietary Reference Intakes for Vitamin A, Vitamin K, Arsenic, Boron, Chromium, Copper, Iodine, Iron, Manganese, Molybdenum, Nickel, Silicon, Vanadium, and Zinc*, National Academies Press, Washington, D **2001**.
- [3] N. F. Krebs, *J. Nutr.* **2000**, *130*, 1374S–1377S.
- [4] The European Commission, *Off. J. Eur. Union: Legis.* **2009**, *52*, L 342, 137.
- [5] T. J. Porea, J. W. Belmont, D. H. Mahoney Jr., *J. Pediatr.* **2000**, *136*, 688–690.
- [6] A. Nel, *Science* **2006**, *311*, 622–627.
- [7] Norm DIN 19378:2004-07, Soil quality - Absorption availability of organic and inorganic pollutants from contaminated soil material, **2004**.
- [8] The National Research Centre for the Working Environment (NRCWE), NANOGENOTOX: Final protocol for producing suitable manufactured nanomaterial exposure media, tech. rep. **2011**.
- [9] J. Teixeira, *J. Appl. Crystallogr.* **1988**, *21*, 781–785.
- [10] R. Ferretti, J. Zhang, J. Buffle, *J. Colloid Interface Sci.* **1998**, *208*, 509–517.
- [11] P. Comodi, S. Nazzareni, P. F. Zanazzi, S. Speziale, *Am. Mineral.* **2008**, *93*, 1530–1537.
- [12] A. Whitaker, *Acta Crystallogr., Sect. A Acta Crystallogr., Sect. B Struct. Crystallogr. Cryst. Chem.* **1975**, *31*, 2026–2035.
- [13] M. C. Hales, R. L. Frost, *Polyhedron* **2007**, *26*, 4955–4962.
- [14] O. Pawlig, R. Trettin, *Mater. Res. Bull.* **1999**, *34*, 1959–1966.
- [15] S. Ghose, *Acta Crystallogr.* **1964**, *17*, 1051–1057.
- [16] M. Römig, C. Feldmann, Y. S. Avadhut, J. Schmedt auf der Günne, *Chem. Mater.* **2008**, *20*, 5787–5795.
- [17] S. Bach, V. R. Celinski, M. Dietzsch, M. Panthöfer, R. Bienert, F. Emmerling, J. Schmedt auf der Günne, W. Tremel, *J. Am. Chem. Soc.* **2015**, *137*, 2285–2294.
- [18] Y. Song, H. Ji, M. Wang, L. He, R. Song, Z. Zhang, *Appl. Surf. Sci.* **2017**, *422*, 228–238.
- [19] J. O. Nriagu, *Geochim. Cosmochim. Acta* **1973**, *37*, 2357–2361.
- [20] A. K. Alwan, P. A. Williams, *Transit. Met. Chem.* **1979**, *4*, 128–132.

- [21] S. Riedel, M. Kaupp, *Coord. Chem. Rev.* **2009**, *253*, 606–624.
- [22] E. Castorina, E. D. Ingall, P. L. Morton, D. A. Tavakoli, B. Lai, *J. Synchrotron Radiat.* **2019**, *26*, 1302–1309.
- [23] P. D'Angelo, A. Zitolo, F. Ceccacci, R. Caminiti, G. Aquilanti, *J. Chem. Phys.* **2011**, *135*, 154509.
- [24] J. Xie, J. Y. Lee, D. I. C. Wang, *J. Phys. Chem. C* **2007**, *111*, 10226–10232.
- [25] S. Zhao, Y. Gao, J. Tan, Y. Zhu, X. Ying, M. Zhang, X. Yu, B. You, *SN Appl. Sci.* **2019**, *1*, 917.
- [26] H. Cölfen, *Nat. Mater.* **2010**, *9*, 960–961.
- [27] D. Gebauer, A. Völkel, H. Cölfen, *Science* **2008**, *322*, 1819–1822.
- [28] B. R. Pauw, A. J. Smith, T. Snow, N. J. Terrill, A. F. Thünemann, *J. Appl. Crystallogr.* **2017**, *50*, 1800–1811.
- [29] J. Filik, A. W. Ashton, P. C. Y. Chang, P. A. Chater, S. J. Day, M. Drakopoulos, M. W. Gerring, M. L. Hart, O. V. Magdysyuk, S. Michalik, A. Smith, C. C. Tang, N. J. Terrill, M. T. Wharmby, H. Wilhelm, *J. Appl. Crystallogr.* **2017**, *50*, 959–966.
- [30] B. Ravel, M. Newville, *J. Synchrotron Radiat.* **2005**, *12*, 537–541.
- [31] L. Voss, P. E. J. Saloga, V. Stock, L. Böhmert, A. Braeuning, A. F. Thünemann, A. Lampen, H. Sieg, *ACS Appl. Nano Mater.* **2020**, *3*, 724–733.
- [32] A. H. Clark, J. Imbao, R. Frahm, M. Nachtegaal, *J. Synchrotron Rad.* **2020**, *27*, 551–557.

Received: May 28, 2020